

High resolution spectroscopy of the high velocity hot post-AGB star LS III +52°24 (IRAS 22023+5249)

G. Sarkar^{1*}, D. A. García-Hernández^{2,3}, M. Parthasarathy^{4,5}, A. Manchado^{2,3,6}
P. García-Lario⁷ and Y. Takeda⁴

¹*Department of Physics, Indian Institute of Technology, Kanpur–208016, U.P., India*

²*Instituto de Astrofísica de Canarias, Vía Láctea s/n, E-38200 La Laguna, Spain*

³*Departamento de Astrofísica, Universidad de La Laguna (ULL), E-38205 La Laguna, Spain*

⁴*National Astronomical Observatory of Japan, 2-21-1 Osawa, Mitaka, Tokyo 181-8588, Japan*

⁵*Aryabhata Research Institute of Observational Sciences, Nainital, 263129, India*

⁶*Consejo Superior de Investigaciones Científicas, Spain*

⁷*Herschel Science Centre. European Space Astronomy Centre. Villafranca del Castillo, P.O. Box 50727. E-28080 Madrid. Spain*

Accepted xx xx xx. Received 2011 xx xx; in original form 2011 xx xx

ABSTRACT

The first high-resolution ($R \sim 50,000$) optical spectrum of the B-type star, LS III +52°24, identified as the optical counterpart of the hot post-AGB candidate IRAS 22023+5249 (I22023) is presented. We report the detailed identifications of the observed absorption and emission features in the full wavelength range (4290–9015 Å) as well as the atmospheric parameters and photospheric abundances (under the Local Thermodynamic Equilibrium approximation) for the first time. The nebular parameters (T_e , N_e) are also derived. We estimate $T_{\text{eff}} = 24,000$ K, $\log g = 3.0$, $\xi_t = 7$ kms^{-1} and the derived abundances indicate a slightly metal-deficient evolved star with $C/O < 1$. The observed P–Cygni profiles of hydrogen and helium clearly indicate on-going post-AGB mass loss. The presence of [N II] and [S II] lines and the non-detection of [O III] indicate that photoionisation has just started. The observed spectral features, large heliocentric radial velocity, atmospheric parameters, and chemical composition indicate that I22023 is an evolved post-AGB star belonging to the old disk population. The derived nebular parameters ($T_e = 7000$ K, $N_e = 1.2 \times 10^4 \text{ cm}^{-3}$) also suggest that I22023 may be evolving into a compact, young low-excitation Planetary Nebula. Our optical spectroscopic analysis together with the recent Spitzer detection of double-dust chemistry (the simultaneous presence of carbonaceous molecules and amorphous silicates) in I22023 and other B-type post-AGB candidates may point to a binary system with a dusty disk as the stellar origin common to the hot post-AGB stars with O-rich central stars.

Key words: Stars: AGB and post-AGB – Stars: early-type – Stars: abundances – Stars: evolution

1 INTRODUCTION

The discovery of high Galactic latitude cool (F, G, K) and hot (O, B) post Asymptotic Giant Branch (post-AGB) supergiants - e.g., HD 161796 (Parthasarathy & Pottasch 1986) and LSII +34°26 (Parthasarathy 1993) - indicated that K, G, F, A, O, B post-AGB supergiants form an evolutionary sequence in the transition region from the tip of the AGB into the early stages of Planetary Nebulae (PNe). Since then, several cool and hot post-AGB candidates have been identified (Pottasch & Parthasarathy 1988; Parthasarathy

& Pottasch 1989; García-Lario et al. 1997a; Parthasarathy et al. 2000a). Gauba & Parthasarathy (2003, 2004) analysed the UV spectra and circumstellar dust envelopes of several hot post-AGB stars from the above lists, including LS III +52°24. Yet to date, the high-resolution ($R \geq 30,000$) optical spectra of only a few hot post-AGB stars have been studied (Sarkar et al. 2005 and references therein). In order to unveil the evolutionary origins, atmospheric parameters, and chemical compositions of hot post-AGB stars, there is a clear need to carry out detailed spectroscopic studies of more examples of this exotic class of post-AGB stars.

The optically bright B-type star, LS III +52°24 identified with the IR source IRAS 22023+5249 (hereafter,

* E-mail: gsarkar@iitk.ac.in

I22023) has far-IR colors similar to PNe (see Table 1). It is listed in Wackerling’s (1970) Catalog of early-type emission-line stars. Recent ground-based high spatial resolution images in the near-IR have shown H₂ emission arising close to the central star, possibly in an incipient bipolar morphology (Volk et al. 2004). Indeed, Kelly & Hrivnak (2005) show that the excitation mechanism of the H₂ emission in I22023 is a combination of radiative (fluorescence) and thermal (shock) excitation. Gauba & Parthasarathy (2004) reported the presence of weak amorphous (10.8 μ m) and crystalline (33.6 μ m) silicate features in the I22023’s Infrared Space Observatory (ISO) spectrum and classified the object as O-rich. However, more recent and higher sensitivity Spitzer/IRS spectra show that I22023 display a mixed-chemistry (both C-rich and O-rich dust features) with the presence of the classical aromatic infrared bands (AIBs; e.g., those at 6.2, 7.7, 8.6, and 11.3 μ m) together with broad 10 μ m amorphous silicate emission and a strong IR excess (Cerrigone et al. 2009).

In this paper, we explore the first high-resolution (R \sim 50,000) optical spectrum of I22023 in order to unveil its evolutionary status and chemical composition and to learn about the stellar origins of this peculiar type of hot post-AGB stars. In Sect. 2 we briefly describe the optical observations of I22023 and the data reduction process. A detailed analysis of the optical spectrum is presented in Sect. 3 while the photospheric and nebular analysis performed are shown in Sect. 4. We finish with a discussion and conclusions in Sect. 5.

2 OBSERVATIONS AND DATA REDUCTION

I22023 was observed on 14 July 2001 using the Utrecht Echelle Spectrograph (UES) on the 4.2m William Herschel Telescope (WHT) at the Roque de los Muchachos Observatory in La Palma (Spain). The observations were made with the 31.6 lines/mm echelle grating (E31), SITe1 CCD (2048 \times 2048 pixels of 24 μ m), a slit width of 1'' on the sky and a central wavelength of 5500 Å, resulting in a resolving power of R \sim 50,000. The wavelength coverage was 4290–4735 Å, 4760–5553 Å and 5607–9015 Å. A Th–Ar comparison lamp was used for wavelength calibration.

The one-dimensional spectrum was extracted using standard reduction procedures for echelle spectroscopy in the IRAF package. The data reduction steps included bias and scattered light subtraction, flat-field correction, order extraction, and wavelength calibration. The reduced spectrum was continuum-normalised. The final signal-to-noise (S/N) ratio varied from 30 in the blue to more than 60 towards the red end of the spectrum.

3 ANALYSIS OF THE OPTICAL SPECTRUM

Equivalent widths (W_λ) of the absorption and emission lines were measured. Deblending was done whenever required to obtain Gaussian fits to the blended line profiles. The complete continuum-normalised spectrum of I22023 is presented in the appendix (Figure 4). This spectrum would be useful for future observers since post-AGB stars show both short and long-term variability in the absorption

and emission line strengths and profiles. P-Cygni profiles detected in these stars are also expected to vary as the stellar wind and post-AGB mass loss rates may show variations as the star evolves. The line identifications are presented in Tables 2 to 5 and are based on the Moore multiplet table (1945) and the linelists of Parthasarathy et al. (2000b), Klochkova et al. (2002) and Sarkar et al. (2005). Unidentified lines are denoted by “UN”. Night sky emission lines denoted by “atmos.” were identified from Osterbrock et al. (1996). The laboratory wavelengths, log (gf) values, and excitation potentials (χ) have been extracted from the Kurucz (CD-ROM 23) linelist GFALL (Moore 1945). Ivan Hubeny and Thierry Lanz have compiled the Kurucz linelists with improved oscillator strengths from the NIST Atomic Spectra Database. For wavelengths below 7500 Å we have used their data which may be retrieved from <http://nova.astro.umd.edu/Synspec43/synspec-frames-data.html>. Note also that in Table 2 the rest wavelengths from Hobbs et al. (2008) are given for the diffuse interstellar bands (DIBs) identified in I22023.

3.1 Description of the spectrum

The absorption and emission lines in the spectrum of I22023 are similar to those detected in other hot post-AGB stars (Parthasarathy et al. 2000b, Klochkova et al. 2002 and Sarkar et al. 2005). In addition to the O I triplet, absorption lines of He I, C II, C III, N II, O II, Ne I, Mg II, Al III, Si III were identified. Emission lines of C II, N II, O I, [O I], Al III, Si II, Fe I, Fe II, [Fe II] and Fe III were also identified in the spectrum of the star. The NaI D1 and D2 lines show a complex structure. The presence of low excitation nebular lines of [N II] and [S II] and the absence of [O III] 5007Å suggest that photoionization has just started, although shock excitation may also be playing a role as indicated by the 40% thermal (shock) excitation to the observed H₂ emission (Kelly & Hrivnak 2005). Balmer lines of H α , H β and H γ show P-Cygni profiles indicating ongoing post-AGB mass loss. Some He I, C II and Fe III lines were also found to have P-Cygni profiles.

3.2 Radial velocity

Heliocentric radial velocities have been derived from wavelength shifts of the well defined absorption and emission lines (Tables 2, 3, 4, and 5). The mean heliocentric radial velocities from the absorption and emission lines (Tables 2 and 3) are -148.31 ± 0.60 km s⁻¹ and -144.13 ± 0.72 km s⁻¹, respectively. Radial velocity measurements of the forbidden lines have been excluded in estimating the mean. The quoted errors refer to the probable errors of estimation. Figure 1 shows the radial velocity trends with respect to the equivalent widths (W_λ) and lower excitation potentials (LEP) of the absorption and emission lines, respectively.

The mean heliocentric radial velocity of the [N II], [O I] and [Fe II] lines is -152.90 ± 0.96 km s⁻¹. [S II] 6717.0Å and 6731.3Å lines in I22023 have a markedly different heliocentric velocity corresponding to -171.93 ± 1.36 km s⁻¹. The different radial velocities argue for a non-spherical nebula.

Table 1. Details of the star

IRAS	Name	RA 2000	DEC 2000	l	b	Sp. Type Optical	V	B–V	IRAS Fluxes (Jy)			
									12 μm	25 μm	60 μm	100 μm
22023+5249	LSIII +52 24	22:04:12.30	+53:04:01.4	99.30	−1.96	B ^a	12.52 ^b	0.69 ^b	1.02	24.69	14.52	3.93L

^aSpectral type is from the SIMBAD database. ^bPhotometry is from Hog et al. (2000). L flag indicates that the quoted IRAS flux density is an upper limit.

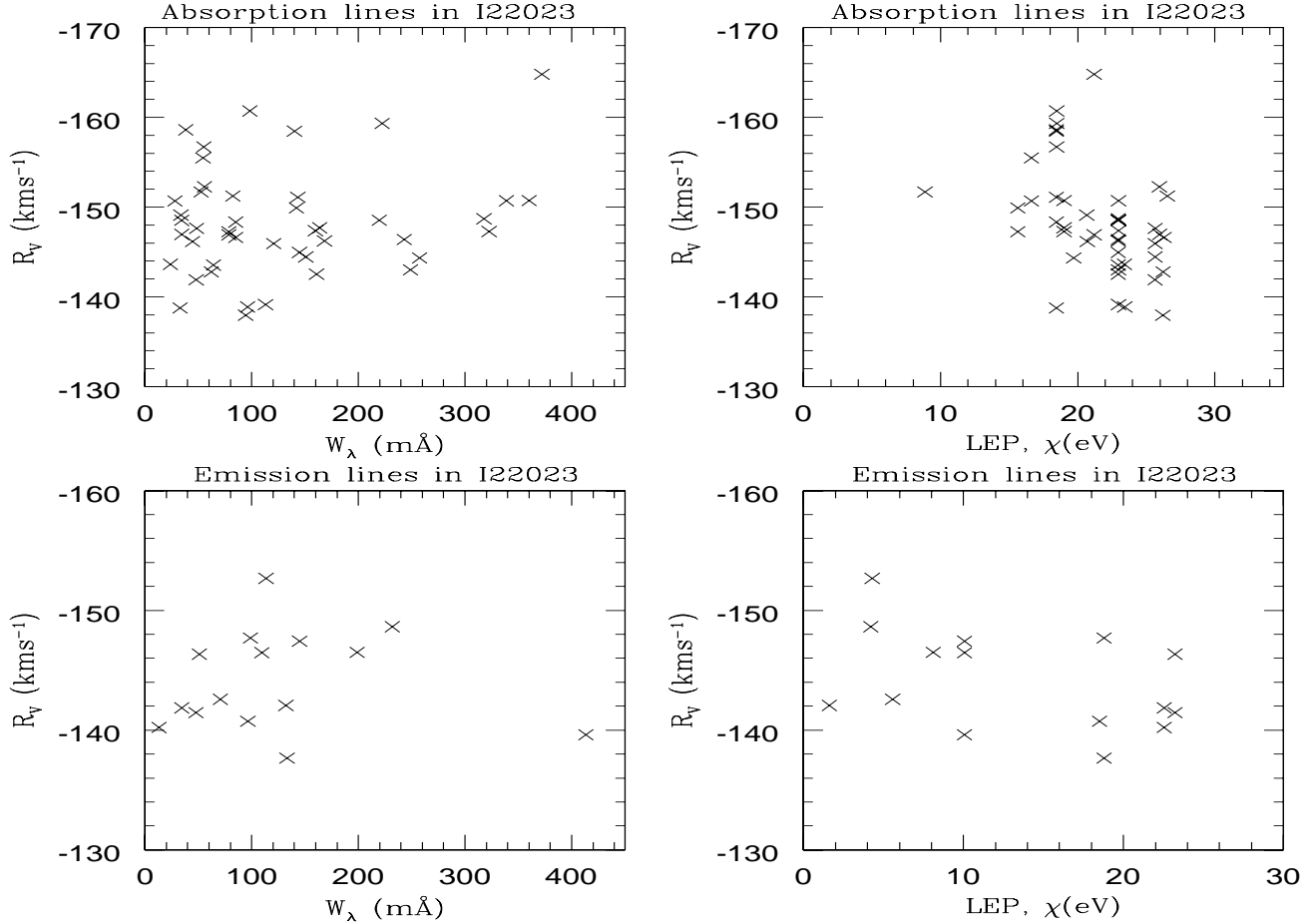


Figure 1. Radial velocity trends of the absorption and emission lines in IRAS22023+5249. Radial velocity measurements of the forbidden lines have not been plotted.

3.3 Wind velocities and mass loss rate from the P–Cygni profiles

The Balmer lines, H_α , H_β , H_γ , a few He I, C II and Fe III lines in I22023 show P–Cygni behaviour (see the appendix and Table 4) indicating ongoing mass–loss. Wind velocities were estimated from the blue absorption edges of the well defined and unblended P–Cygni profiles (Table 4). The wind velocities of the Fe III(5) lines are markedly different from those of the other species. However, the wind velocities do not show any obvious trend with the lower excitation potentials or ionization potentials of the species. The mean wind velocity from the Balmer, He I and C II lines is 187.48 kms^{-1} and that from the Fe III(5) lines is 149.26 kms^{-1} . This difference in velocities indicates a deviation from spherical sym-

metry – possibly a bipolar morphology and the presence of a dense equatorial torus (e.g., Welch et al. 1999; Sahai et al. 2005). Only very high-spatial resolution ($\text{FWHM} < 0.15''$) images (e.g., using the Hubble Space Telescope) may reveal the true morphology of the object.

The Balmer lines H_α , H_β , and H_γ in I22023 are shown in Figure 2 where the velocities are in the heliocentric frame. A more detailed modelling of these lines to derive the mass loss rate is out of the scope of this paper. The equivalent widths of the H_α emission components are related to the mass loss rates in OB stars (Leitherer 1988). The H_α emission component in I22023 has an equivalent width ($W_\lambda = 37.8 \text{\AA}$) comparable to that of the O8I star, HD152408 ($W_\lambda = 34.7 \text{\AA}$). From this, we estimate a mass loss rate of $1.23 \times 10^{-5} \text{ M}_\odot \text{yr}^{-1}$.

Table 2. Absorption lines in IRAS 22023+5249^a

$\lambda_{\text{obs.}}$ (Å)	$\lambda_{\text{lab.}}$ (Å)	Ident.	W_{λ} (Å)	$\log(gf)$	χ (eV)	$ \Delta\lambda $ (Å)	V_r km s ⁻¹
4314.874	4317.139	OII(2)	0.1609	-0.386	22.95-25.82	2.265	-142.53
4317.277	4319.630	OII(2)	0.2197	-0.380	22.96-25.83	2.353	-148.55
4343.245	4345.560	OII(2)	0.1448	-0.346	22.96-25.81	2.315	-144.95
4345.141	4347.413	OII(16)	0.0480	0.024	25.64-28.49	2.272	-141.91
4347.137	4349.426	OII(2)	0.2489	0.060	22.98-25.83	2.289	-143.01
4348.903	4351.260	OII(16)	0.0483	0.227	25.64-28.49	2.357	-147.64
4364.653	4366.895	OII(2)	0.1130	-0.348	22.98-25.82	2.242	-139.15
4385.301	4387.929	HeI(51)	0.3722	-0.883	21.20-24.03	2.628	-164.80
4412.525	4414.899 ^b	OII(5)		0.172	23.42-26.23		blend
4414.702	4416.975 ^c	OII(5)	0.1319	-0.077	23.40-26.21	2.384	blend
4435.158	4437.551	HeI(50)	0.0786	-2.034	21.20-23.99	2.393	-146.91
4478.638	4479.885	AlIII(8)	0.0524	0.900	20.77-23.53		
	+ 4479.971	AlIII(8)		1.020	20.77-23.53		
	+ 4481.126	MgII(4)		0.740	8.86-11.62	2.488	-151.70
4550.109	4552.622	SiIII(2)	0.3600	0.181	19.00-21.72	2.513	-150.73
4565.371	4567.840	SiIII(2)	0.3225	-0.039	19.00-21.72	2.469	-147.28
4572.278	4574.757	SiIII(2)	0.1638	-0.509	19.00-21.71	2.479	-147.70
4588.513	4590.974	OII(15)	0.1206	0.350	25.64-28.34	2.461	-145.95
4593.736	4596.177	OII(15)	0.1507	0.200	25.64-28.34	2.441	-144.46
4627.829	4630.539	NII(5)	0.0983	0.094	18.47-21.14	2.710	-160.70
4636.365	4638.856	OII(1)	0.1682	-0.332	22.95-25.62	2.491	-146.23
4639.279	4641.810	OII(1)	0.3179	0.055	22.96-25.63	2.531	-148.71
4644.997	4647.418	CIII(1)	0.1181	0.070	29.51-32.18	2.421	-141.41
4646.569	4649.135	OII(1)	0.3387	0.308	22.98-25.65	2.566	-150.71
4648.297	4650.16	CIII(1)	0.2709				blend
	+ 4650.841	OII(1)					
	+ 4651.35	CIII(1)					
4659.126	4661.632	OII(1)	0.2431	-0.278	22.96-25.62	2.506	-146.40
4671.265	4673.733	OII(1)	0.0644	-1.090	22.96-25.61	2.468	-143.55
4673.706	4676.235	OII(1)	0.1598	-0.394	22.98-25.63	2.529	-147.38
4693.804	4696.353	OII(1)	0.0346	-1.380	22.98-25.62	2.558	-148.53
4696.824	4699.218	OII(25)	0.0944	0.270	26.21-28.84	2.394	-137.96
4702.873	4705.346	OII(25)	0.0621	0.477	26.23-28.86	2.473	-142.80
4817.027	4819.712	SiIII(9)	0.0556	0.750	25.96-28.53	2.685	-152.26
4826.346	4828.951	SiIII(9)	0.0344	1.090	25.97-28.53	2.605	-146.97
4904.197	4906.830 ^d	OII(28)		-0.161	26.29-28.81	2.633	-146.11
4918.616	4920.35	HeI(49)	0.4414		21.13-23.64		blend
	+ 4921.931	HeI(48)		-0.435	21.20-23.72		
4921.878	4924.529	OII(28)	0.0851	0.074	26.29-28.80	2.651	-146.63
4940.268	4943.005	OII(33)	0.0825	0.239	26.54-29.05	2.737	-151.24
5000.141	5002.703	NII(4)	0.0328	-1.022	18.45-20.92	2.562	-138.77
5002.414	5005.150	NII(19)	0.0336	0.594	20.65-23.13	2.736	-149.12
5007.895	5010.621	NII(4)	0.0851	-0.607	18.45-20.92	2.726	-148.34
5042.253	5044.8	CII(35)	0.1148				blend
	+ 5045.098	NII(4)					
5044.65	5047.2	CII(35)	0.0825				blend
	+ 5047.736	HeI(47)					
5130.277	5132.947	CII(16)	0.0376	-0.211	20.69-23.10		blend
	+ 5133.282	CII(16)		-0.178	20.69-23.10		
5140.722	5143.495	CII(16)	0.0640	-0.212	20.69-23.10		blend
5142.407	5145.165	CII(16)	0.0523	0.189	20.70-23.10		blend
5148.32	5151.085	CII(16)	0.0446	-0.179	20.70-23.10	2.765	-146.16
5216.486		UN	0.0471				
5486.97	5487.69	DIB	0.0343			0.460	-10.28
5663.356	5666.630	NII(3)	0.1400	-0.045	18.45-20.64	3.274	-158.46
5672.88	5676.02	NII(3)	0.1433	-0.367	18.45-20.63	3.14	-151.09
5676.262	5679.56	NII(3)	0.2223	0.250	18.47-20.65	3.298	-159.33
5682.922	5686.21	NII(3)	0.0382	-0.549	18.45-20.63	3.288	-158.60

Table 2. Absorption lines in IRAS 22023+5249^a. contd..

$\lambda_{\text{obs.}}$ (Å)	$\lambda_{\text{lab.}}$ (Å)	Ident.	W_{λ} (Å)	$\log(gf)$	χ (eV)	$ \Delta\lambda $ (Å)	V_r km s ⁻¹
5693.475	5695.920	CIII(2)	0.1418	0.017	32.08–34.26		
	+ 5696.604	AlIII(2)		0.230	15.63–17.81	3.129	–149.91
5707.504	5710.770	NII(3)	0.0552	–0.518	18.47–20.64	3.266	–156.70
5719.637	5722.730	AlIII(2)	0.0786	–0.070	15.63–17.80	3.093	–147.27
5736.688	5739.734	SiIII(4)	0.2575	–0.160	19.71–21.87	3.046	–144.34
5779.728	5780.480	DIB	0.3405			0.682	–20.52
5796.444	5797.060	DIB	0.0440			0.586	–15.46
6139.673	6143.063	NeI(1)	0.0282	–0.350	16.61–18.62	3.39	–150.68
6195.200	6195.980	DIB	0.0756			0.790	–23.38
6202.191	6203.050	DIB	0.0966			0.869	–27.16
6269.073	6269.850	DIB	0.0691			0.777	–22.50
6282.734	6283.840 ^e	DIB	0.7319			1.126	–38.89
6398.61	6402.246	NeI (1)	0.0543	0.360	16.61–18.54	3.636	–155.48
6612.857	6613.620	DIB	0.1268			0.773	–20.19
6637.522	6641.031	OII(4)	0.0238	–0.884	23.40–25.27	3.509	–143.64
6717.943	6721.388	OII(4)	0.0963	–0.610	23.43–25.27	3.445	–138.89
7766.623	7771.944	OI(1)	0.576	0.320	9.14–10.74		blend
7769.416	7774.166	OI(1)	0.434	0.170	9.14–10.74		blend
	+ 7775.388	OI(1)		–0.050	9.14–10.74		
8592.524		UN	0.265				
8646.868	8648.280	DIB	0.466			1.412	–34.11

^a Note that the rest wavelengths from Hobbs et al. (2008) are given for the DIBs. ^bOII(5) 4414.899 Å is blended with FeII(32) Å emission. ^cOII(5) 4416.975 Å is blended with the absorption component of FeIII(114) 449.596 P–Cygni profile. ^dOII(28) 4906.88 Å is blended with [FeII](20F) 4905.35 Å emission. ^eDIB 6283.84 Å is blended with telluric absorption lines in this region.

(Leitherer 1988). However, the Leitherer (1988)’s method is valid for massive stars and it may be not applicable for hot post-AGB supergiants. Therefore the mass loss rate estimated for I22023 may be not correct and hence it should be used with caution. Also, in I22023, the large equivalent width of the H α emission component may be due to a large amount of gas in its circumstellar envelope or to the presence of a possible bipolar envelope (Volk et al. 2004) and may not be directly related to the mass loss rate.

3.4 Diffuse interstellar bands (DIBs)

Diffuse interstellar bands (DIBs) at 5487.69 Å, 5780.48 Å, 5797.06 Å, 6195.98 Å, 6203.05 Å, 6269.85 Å, 6283.84 Å, 6613.620 Å, etc. (Hobbs et al. 2008) were identified in the spectrum of the star (see Table 2). DIBs were also detected in the spectra of several other hot post-AGB stars such as IRAS 01005+7910 (Klochova et al. 2002), IRAS 13266–5551, and IRAS 17311–4924 (Sarkar et al. 2005). Some of us presented a detailed analysis of the most famous DIBs in the spectrum of I22023 and in the spectra of several other post-AGB stars (Luna et al. 2008). Luna et al. (2008) found that the DIBs’ strength in post-AGB stars is consistent with the interstellar extinction toward these sources. This implies that DIBs are not originated in the circumstellar shells of post-AGB stars. Thus, we estimate an interstellar E(B–V)=0.67 from the measured equivalent width of 0.3405 Å for the 5780 Å DIB and the correlation measured by Friedman et al. (2011). As we have mentioned before, a more detailed analysis of DIBs in post-AGB stars can be found in the paper by Luna et al. (2008).

3.5 Na I D₂ and Na I D₁ lines

Six components were identified in the Na I D₂ and Na I D₁ lines (see Figure 3 and Table 5). The velocities of absorption component 1 and emission component 2 are comparable with the mean heliocentric radial velocities of the absorption and emission lines in the star (Sect. 3.2) suggesting that component 1 is of photospheric origin and component 2 arises in an extended envelope around the central star. Comparing the heliocentric velocities of absorption components 3, 4, and 5 with those of DIBs observed in the spectrum of the star we may infer that these components originate in the interstellar medium. Component 6 is observed in emission with a velocity very different from the envelope velocity. This component may arise in a disk or in outflows around the central star. The velocity of this component is comparable with the expansion velocity estimated from the nebular lines (Sect. 4.2).

4 ANALYSIS OF THE ABSORPTION AND EMISSION LINE SPECTRA

4.1 Atmospheric parameters and abundances from absorption line spectrum

The detection of He I and Si III absorption lines in addition to the C III lines and the absence of He II absorption lines, indicates a B0 – B1 supergiant spectral type for the central star. A previous comparison of the UV(IUE) spectrum of I22023 with standard stars suggested that the star was similar to a B2–supergiant (Gauba & Parthasarathy 2003).

Table 3. Emission lines in IRAS 22023+5249

$\lambda_{\text{obs.}}$ (Å)	$\lambda_{\text{lab.}}$ (Å)	Ident.	W_λ (Å)	log (gf)	χ (eV)	$ \Delta\lambda $ (Å)	V_r km s ⁻¹
4411.134	4413.601 ^a	FeII(32)	0.0600	-3.870	2.67–5.48		blend
4811.856	4814.55	[FeII](20F)	0.0409			2.694	-153.00
4902.59	4905.35 ^b	[FeII](20F)	0.0287				blend
5038.313	5041.024	SiII(5)	0.1095	0.291	10.06–12.52	2.711	-146.47
5053.306	5055.984	SiII(5)	0.2758	0.593	10.07–12.52		blend
	+ 5056.317	SiII(5)		-0.359	10.07–12.52		
5088.76		UN	0.0244				
5155.834	5158.81	[FeII](19F)	0.0985				blend
5191.418	5193.909	FeIII(5)	0.0594	-2.852	8.65–11.04		blend
	+ 5194.384	FeIII(5)			8.65–11.04		
5195.026	5197.929	FeI(1091)	0.1135	-1.640	4.30–6.68	2.903	-152.68
5197.427		UN	0.084				
5232.982		UN	0.0412				
5240.659	5243.306	FeIII(113)	0.0997	0.405	18.26–20.62		blend
	+ 5243.773	FeI(1089)		-1.150	4.25–6.62		
5258.712	5261.61	[FeII](19F)	0.0520			2.898	-150.36
5270.327	5273.38	[FeII](18F)	0.0481			3.053	-158.81
5273.648		UN	0.0487				
5279.665		UN	0.0756				
5282.071		UN	0.0277				
5286.85		UN	0.0632				
5296.105	5299.044	OI(26)	0.1163	-2.140	10.98–13.32		blend
5297.325		UN	0.0366				
5299.853		UN	0.0368				
5751.43	5754.8	[NII](3F)	0.0436				weak
5830.998	5834.06	FeII(165)	0.0705	-3.738	5.57–7.69	3.062	-142.58
5917.114	5920.124	FeIII(115)	0.1332	-0.034	18.78–20.87	3.01	-137.66
5926.609	5929.685	FeIII(114)	0.0964	0.351	18.50–20.59	3.076	-140.75
5950.424	5953.613	FeIII(115)	0.0989	0.186	18.78–20.86	3.226	-147.69
5954.336	5957.559	SiII(4)	0.1449	-0.301	10.06–12.14	3.223	-147.43
5975.851	5978.930	SiII(4)	0.4134	0.004	10.07–12.14	3.079	-139.62
5996.369	5999.70	AlII(93)	0.1843		15.52–17.57		blend
	+ 5999.83	AlII(93)			15.52–17.57		
6029.382	6032.67	FeI(1082)	0.2320		4.20–6.25	3.288	-148.64
6043.111	6046.233	OI(22)	0.0968	-1.895	10.98–13.03		blend
	+ 6046.438			-1.675	10.98–13.03		
6092.139	6095.290	CII(24)	0.0131	-0.029	22.55–24.58	3.151	-140.22
6095.324	6098.510	CII(24)	0.0344	0.226	22.56–24.59	3.186	-141.86
6146.784	6150.10	FeII(46)	0.0292		3.21–5.21		blend
6148.099		UN	0.0828				
6296.769	6300.23	[OI](1F)	0.2832			3.461	-149.93
6337.276	6340.58	NII(46)	0.0479	-0.192	23.23–25.18	3.304	-141.46
6343.686	6346.86	NII(46)	0.5132	-0.901	23.22–25.18		blend
	+ 6347.109	SiII(2)		0.297	8.12–10.07		
6353.584	6357.0	NII(46)	0.0511		23.23–25.18	3.416	-146.34
6360.279	6363.88	[OI](1F)	0.0677			3.601	-154.89
6367.944	6371.371	SiII(2)	0.1989	-0.003	8.12–10.06	3.427	-146.49
6458.428		UN	0.1059				
6544.492	6548.1	[NII](1F)	2.817			3.608	-150.43
6579.838	6583.6 ^c	[NII](1F)	8.534				blend
6712.772	6717.0	[SII](2F)	0.5017			4.228	-173.96
6727.154	6731.3	[SII](2F)	1.007			4.146	-169.91
6848.05	6851.634	FeI(34)	0.1321	-5.320	1.61–3.41	3.584	-142.06
6998.28	7001.93	OI(21)	0.0786		10.94–12.70		blend
	+ 7002.22	OI(21)			10.94–12.70		
	7231.330 ^d	CII(3)		0.043	16.32–18.03		blend
	7236.420 ^d	CII(3)		0.299	16.32–18.03		blend
	7316.282 ^d	atmos.					
7373.821		UN	0.1893				

Table 3. Emission lines in IRAS 22023+5249. contd.

$\lambda_{\text{obs.}}$ (Å)	$\lambda_{\text{lab.}}$ (Å)	Ident.	W_{λ} (Å)	log (gf)	χ (eV)	$ \Delta\lambda $ (Å)	V_r km s ⁻¹
7458.676		UN	0.1119				
7462.426		UN	0.1229				
7464.227		UN	0.122				
7892.292		UN	0.134				
7993.283	7993.332	atmos.	0.0534				
8218.700	8223.128 ^d	NI(2)		-0.390	10.32–11.83		blend
8237.897	8242.389 ^d	NI(2)		-0.380	10.33–11.83		blend
8283.265		UN					blend
8441.864	8446.359	OI(4)	3.097	0.170	9.51–10.98		blend
	+ 8446.758	OI(4)		-0.050	9.51–10.98		
8745.796 ^d		UN					
8857.744 ^d		UN					

^aFeII(32) 4413.601Å is blended with OII(5) 4414.899Å absorption feature. ^b[FeII](20F) 4905.35Å is blended with OII(28) 4906.88Å absorption feature. ^c[NII](1F) 6583.6Å is blended with the emission component of CII(2) 6582.88Å P–Cygni profile. ^dThese emission lines are weak and are blended with the atmospheric absorption lines in this region.

Table 4. P–Cygni lines in IRAS22023+5249. Equivalent widths of the absorption and emission components of the P–Cygni profiles are given. Wind velocities are estimated from the blue absorption edges of the P–Cygni profiles.

λ_{lab} (Å)	Ident.	W_{λ} (absorption) (Å)	W_{λ} (emission) (Å)	log (gf)	χ (eV)	Wind Velocity km s ⁻¹
4340.462	H $_{\gamma}$	0.4908	1.915	-0.447	10.19–13.04	-187.81
4419.596 ^a	FeIII(4)	0.0991	0.0987	-2.218	8.23–11.04	blend
4431.019	FeIII(4)	0.0429	0.0506	-2.572	8.24–11.04	weak
4471.477	HeI(14)	0.3398	0.0828		20.95–23.72	blend
+4471.682 ^c	HeI(14)			-0.898	20.95–23.72	
4861.323 ^b	H $_{\beta}$	0.1235	6.779	-0.020	10.19–12.74	-192.63
5015.678	HeI(4)	0.3955	0.5047	-0.820	20.60–23.07	-185.39
5073.903	FeIII(5)	0.1361	0.0426	-2.557	8.65–11.09	weak
5086.701	FeIII(5)	0.0319	0.0338	-2.590	8.65–11.09	weak
5127.387	FeIII(5)	0.1048	0.1684	-2.218	8.65–11.07	-149.39
5156.111	FeIII(5)	0.1105	0.1964	-2.018	8.64–11.04	-149.14
5875.618	HeI(11)	0.5500	1.8790		20.87–22.97	blend
+ 5875.650 ^c	HeI(11)				20.87–22.97	
+ 5875.989 ^c	HeI(11)				20.87–22.97	
6562.797 ^b	H $_{\alpha}$	0.0443	37.86	0.710	10.19–12.08	-185.36
6578.050	CII(2)	0.1977	0.2779	-0.026	14.44–16.32	-191.55
6582.880 ^d	CII(2)			-0.327	14.43–16.32	blend
6678.154	HeI(46)	0.6693	0.8538	0.329	21.20–23.06	-182.16
7065.176	HeI(10)	0.3406	1.3600	-0.460	20.95–22.70	blend
+ 7065.707 ^c	HeI(10)			-1.160	20.95–22.70	

^aThe absorption component of FeIII(114) 4419.596Å is blended with OII(5) 4416.975 absorption feature.

^bThe emission components of the H $_{\beta}$ and H $_{\alpha}$ profiles have broad wings. Gaussian fits to the absorption and emission components of these profiles could not be obtained. Using IRAF, the equivalent widths of these components were estimated by subtracting the linear continuum between the points of interest and summing the pixels with partial pixels at the ends. ^cCII(2) 6582.88Å P–Cygni profile is blended with [NII](1F) 6583.6Å.

Similarly to our previous analysis of the high-resolution optical spectrum of the hot post–AGB star IRAS 13266–5551 (Sarkar et al. 2005), we have used the Kurucz’s WIDTH 9 program and the spectrum synthesis code SYNSPEC (Hubeny et al. 1985) together with solar metallicity Kurucz (1994) model atmospheres to derive the atmospheric parameters and elemental abundances of I22023 under the Local Thermodynamic Equilibrium (LTE) approximation.

The largest number of absorption lines in I22023 are those of O II and N II. We derived the oxygen and nitrogen abundance with the WIDTH 9 program for various combinations of effective temperature (T_{eff}), gravity (log g), and microturbulence (ξ_t). We covered 18,000 K $\leq T_{\text{eff}} \leq$ 25,000 K and 5 $\leq \xi_t \leq$ 10 kms⁻¹. From the Kurucz (1994) model atmospheres, the log g value was limited to a minimum of 3.0. For each combination of these parameters, we then syn-

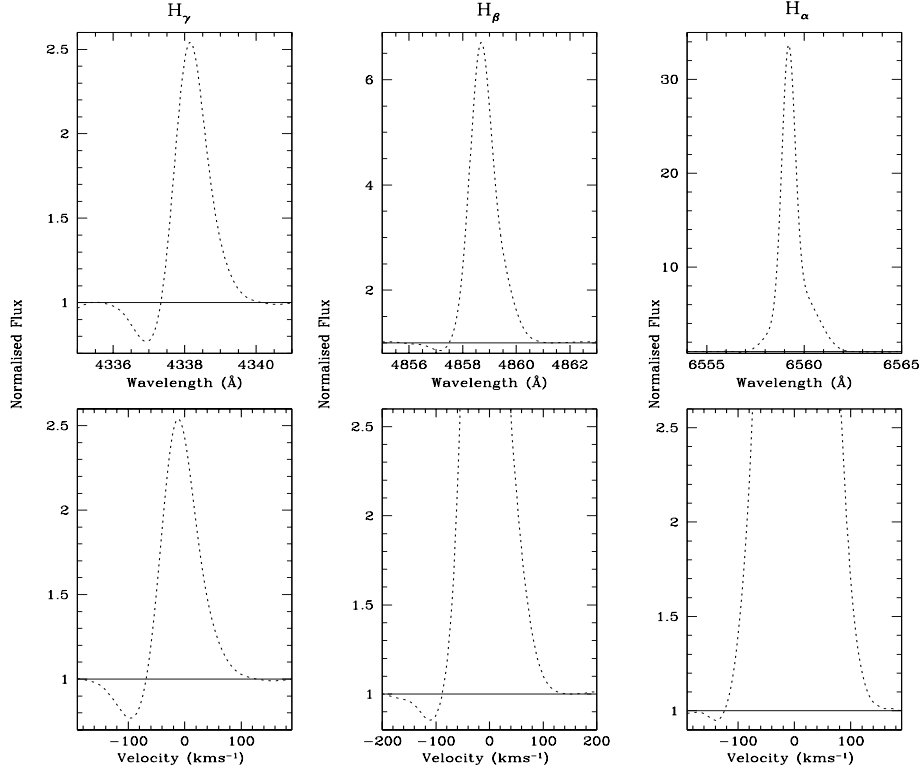


Figure 2. Observed Balmer H_γ , H_β , and H_α profiles (dotted) in I22023, showing P-Cygni behaviour. Note that the velocities are in the heliocentric frame.

Table 5. Absorption (a) and emission (e) components of Na I D₂ (5889.953 Å) and Na I D₁ (5895.923 Å) lines in the spectrum of IRAS22023+5249 (LSIII +5224). W_λ are the equivalent widths of the components and V_r are the respective heliocentric radial velocities.

Component		IRAS22023+5249					
		Na I D ₂			Na I D ₁		
		$\lambda_{\text{obs.}}$ (Å)	W_λ (Å)	V_r (km s ⁻¹)	$\lambda_{\text{obs.}}$ (Å)	W_λ (Å)	V_r (km s ⁻¹)
1.	a	5886.341	0.0559	-169.10	5892.323	0.0529	-168.31
2.	e	5886.811	0.1314	-145.17	5892.763	0.0277	-145.92
3.	a	5888.530	0.1395	-57.61	5894.500	0.1355	-57.54
4.	a	5888.903	0.5054	-38.61	5894.881	0.3684	-38.15
5.	a	5889.500	0.6384	-8.20	5895.455	0.6241	-8.94
6.	e	5889.918	0.1221	+13.09	5895.902	0.1471	+13.8

thesised the spectrum using SYNSPEC. The best fit to the observed spectrum was obtained for $T_{\text{eff}} = 24,000 \pm 1000$ K, $\log g = 3.0 \pm 0.5$, $\xi_t = 7 \pm 1$ km s⁻¹. Since strong lines are usually affected by microturbulence, the use of these lines in determining the atmospheric parameters of the star may contribute to systematic errors. Thus, we excluded lines with $W_\lambda \geq 200$ mÅ in our estimation of the atmospheric parameters and abundances. Line blends were also excluded from our analysis. Final abundances for He, C, N, O, Ne, and Si are summarized in Table 6. The estimated errors in the derived abundances taking into account typical variations in the atmospheric parameters are listed in Table 7.

4.1.1 He I lines

Several absorption and P-Cygni type He I lines were identified in the spectrum of I22023. The absorption lines are blends with the exception of the strong 4387.929 Å He I(51) ($W_\lambda=372.2$ mÅ) line and the He I(50) 4437.551 Å line ($W_\lambda=78.6$ mÅ). For the derived atmospheric parameters of the star, and by using spectrum synthesis, we estimated the helium abundance from the He I(50) line (see Table 6).

4.1.2 C II and C III lines

Both C II and C III absorption lines were detected in the spectrum of the star. However, the number of these lines in

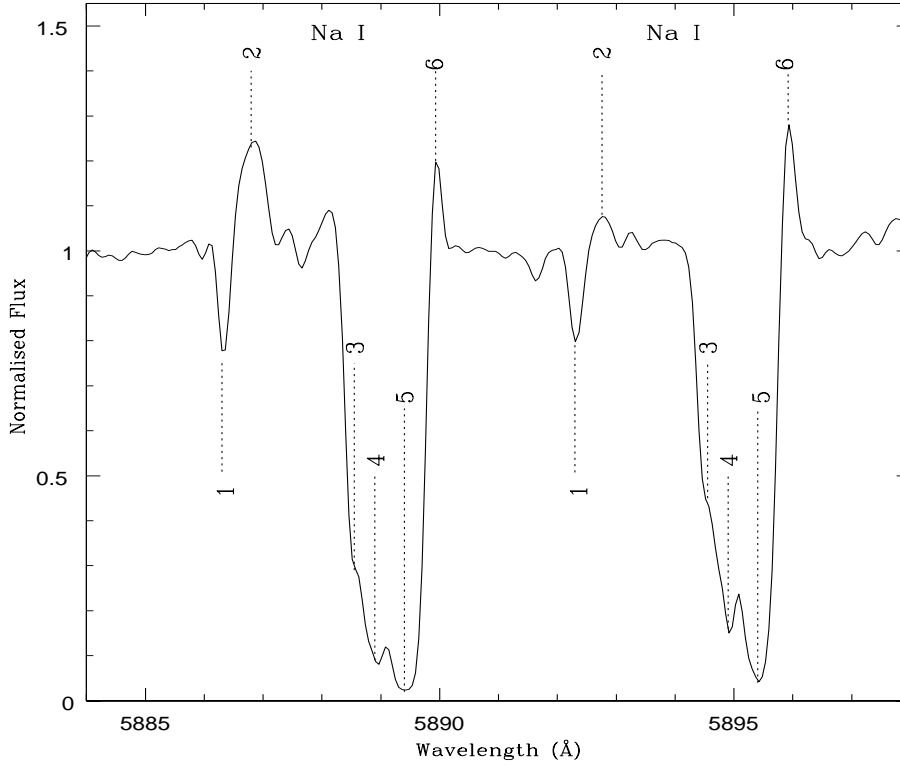


Figure 3. Na I D₂ and Na I D₁ lines in I22023. The various absorption and emission components (Sect. 3.5, Table 5) have been labelled.

Table 6. Derived abundances for I22023. The values are for $\log \epsilon(\text{H}) = 12.0$. n refers to the number of lines of each species used for the abundance determination. For comparison we have listed the solar abundances ($\log \epsilon(\text{X})_{\odot}$) and average abundances for main sequence B-stars from the Ori OB1 association (Kilian, 1992).

X	IRAS22023+5249 ($T_{\text{eff}}=24000$ K, $\log g=3.0$, $\xi_t=7$ km s ⁻¹)				Main sequence B-stars, Ori OB1	
	n	$\log \epsilon(\text{X})$	σ	[X/H]	$\log \epsilon(\text{X})_{\odot}$	$\log \epsilon(\text{X})$
He I	1	11.04 [†]	—	+0.11	10.93	11.04
C II	4	8.58 [†]	—	+0.19	8.39	8.23
N II	7	8.36	0.33	+0.44	7.92	7.72
O II	18	8.90	0.42	+0.21	8.69	8.60
Ne I	2	9.02	0.14	+0.94	8.08	—
Al III	1	< 6.79 [†]	—	—	6.47	—
Si III	3	7.43	0.59	-0.12	7.55	—

The abundances were derived using Kurucz's WIDTH9 program.

[†]These values were derived from spectrum synthesis analysis using the SYNSPEC code.

Table 7. Uncertainties in the derived abundances, $\Delta \log \epsilon(\text{X})$, due to uncertainties in the model atmospheric parameters

Element	ΔT_{eff} -1000K	$\Delta \log g$ +0.5	$\Delta \xi_t$ +1 km s ⁻¹	σ_m
N	-0.14	-0.18	-0.05	0.23
O	+0.05	+0.08	-0.08	0.12
Ne	-0.15	-0.26	-0.01	0.30
Si	-0.04	-0.06	-0.07	0.10

I22023 is low. Furthermore, all the identified carbon lines are blends with the exception of the C II(16) line at 5151.085 Å. The carbon abundance was therefore estimated using spectrum synthesis only. The region of the C II(16) lines ($\sim 5132\text{--}5151$ Å) was used for this purpose.

4.1.3 O II lines and the O I triplet

The largest number of absorption lines in the I22023's spectrum are those of O II. The O II lines with $W_\lambda \geq 200$ mÅ may be sensitive to non-LTE effects and such strong O II lines were not considered in our oxygen abundance estimation by using the WIDTH9 program. For the derived atmospheric parameters and the oxygen abundance of $\log \epsilon(\text{O})=8.90$, we could not obtain a perfect fit to the stronger O II lines with the SYNSPEC code.

On the other hand, the (total) equivalent width of the O I triplet in the spectrum of I22023 is 1.01 Å. This is comparable to the 0.95 Å equivalent width of the O I triplet in the spectrum of the B1.5Ia hot post-AGB star, LSII+34°26 (García-Lario et al. 1997b; Arkhipova et al. 2001). The O I triplet at 7773 Å is known to be sensitive to non-LTE effects. Indeed, we could not obtain a good fit to the O I triplet by assuming the oxygen abundance ($\log \epsilon(\text{O})=8.90$) derived from the O II lines (Table 6).

4.1.4 N II and Ne I lines

Several N II and two Ne I lines were identified in I22023. The abundances of these lines were estimated using WIDTH9. Again, the stronger N II lines with $W_\lambda \geq 200$ mÅ were not taken into account in our estimation ($\log \epsilon(\text{N})=8.36$) of the nitrogen abundance in I22023.

4.1.5 Metallic lines

Only one Mg II line could be identified in the spectrum of the star. This line is blended with Al III(8). Since the Al III abundance in I22023 is uncertain (see below), we did not attempt to estimate the magnesium abundance from the blended 4481.126 Å Mg II(4) line. Also, four Al III lines could be identified in I22023. Three of these lines are clear blends with other atomic species. Therefore, we estimated the aluminium abundance from the single 5722.730 Å Al III(2) line by using spectrum synthesis and we derived $\log \epsilon(\text{Al})=6.79$. This abundance from a single line with $W_\lambda=78.6$ mÅ may be treated as an upper limit. The silicon abundance ($[\text{Si}/\text{H}]=-0.12$) was derived by using three Si III line and suggests that I22023 may be slightly metal deficient. Finally, it is to be noted here that the iron abundance could not be estimated since the iron lines in I22023 appear only in emission or show P-Cygni profiles.

4.1.6 Uncertainties in the abundance determinations

The standard deviation (σ) which measures the scatter in the abundances due to individual lines of a particular species was estimated using WIDTH9 (Table 6). The true error, σ/\sqrt{n} , would be smaller for species with a greater number of lines (n). Table 7 gives the uncertainties in the abundances due to typical uncertainties in the model atmospheric

parameters taken for the modelling: $\Delta T_{\text{eff}}=-1000\text{K}$, $\Delta \log g=+0.5$, and $\Delta \xi_t=+1 \text{ km s}^{-1}$. Thus, the formal error (always ≤ 0.3 dex) in the derived abundances is the quadratic sum of the uncertainties introduced by typical variations of the atmospheric parameters and it is given by σ_m in Table 7.

4.2 Analysis of the emission line spectrum

Several permitted and forbidden emission lines were identified in the spectrum of the star and are listed in Table 3. Nebular parameters and expansion velocities were determined using the forbidden lines (see below).

4.2.1 Nebular parameters

In the absence of a flux calibrated spectrum for I22023, it is not possible to obtain the absolute fluxes in the observed emission lines. However, reliable emission line flux ratios may be deduced by combining the observed equivalent widths (Table 3) with estimates of the stellar continuum flux distribution in the regions of the emission lines. The latter were obtained for the derived atmospheric parameters of the star (Sect. 4.1) by using the SYNSEPC code and the Kurucz model atmospheres. The emission line fluxes thus estimated are free from the effects of both interstellar and circumstellar reddening.

The [S II] $\lambda 6717/\lambda 6731$ line ratio is an electron density diagnostic and the [N II] ($\lambda 6548+\lambda 6583$)/ $\lambda 5755$ line ratio is sensitive to electron temperature. In I22023, the [N II] 6583.6 Å emission is blended with the emission component of the C II(2) 6582.88 Å P-Cygni profile. However, comparing the 6582.88 Å C II(2) profile with the 6578.05 Å C II(2) P-Cygni profile (see the appendix), we may conclude that the contribution of C II(2) to the [N II] emission profile is negligible. Using the NEBULAR analysis package under IRAF, we obtained T_e vs. N_e contours for the observed [S II] and [N II] diagnostic ratios of 0.5 and 166.7, respectively. From the intersection of the contours we obtained $T_e=7,000$ K and $N_e=1.2 \times 10^4 \text{ cm}^{-3}$. The high electron density is comparable to that measured in the very young and compact PN Hen3-1357 (Parthasarathy et al. 1993; Bobrowsky et al. 1998) which evolved from the hot post-AGB stage into a PN in the 20–30 yrs (Parthasarathy et al. 1995).

Unfortunately, we could not derive the nebular C, N, and O abundances, which could then have been compared with the photospheric abundances to estimate the amount of material lost by the star during nebular formation and the chemical composition of the nebula. Such a calculation requires an estimate of the H_β emission line flux. However, H_β in I22023 shows a P-Cygni profile and it is not possible to estimate the nebular emission from this profile.

4.2.2 Expansion velocities

Expansion velocities were estimated from the FWHM of the unblended [O I], [N II] and [S II] lines using $V_{\text{exp}}=0.50$ FWHM (see Table 8). Note that the [N II](1F) 6583.6 Å line is blended with the emission component of C II(2) 6582.88

Å P-Cygni profile and has not been used to estimate the expansion velocity.

This approximation is valid when emission is confined to a thin spherically symmetric shell. However, I22023 appears to have an incipient bipolar morphology in recent ground-based high spatial (FWHM \sim 0.15") resolution images (Volk et al. 2004). Furthermore, the observed [O I] 6300.23 Å and 6363.88 Å line profiles appear to be asymmetric. Though no obvious line split is observed in the weak [O I] lines, their asymmetric nature may indicate the presence of a red and a blue component. This may explain the discrepancy between the expansion velocities estimated from [O I], [N II], [S II] lines in I22023, the former being nearly twice that of the latter two species. The mean nebular velocity based on the [N II] and [S II] lines is 17.5 km s $^{-1}$.

The possible bipolar morphology of this object is not completely established (Volk et al. 2004). In addition, Cerrigone et al. (2008) studied the radio continuum emission of this object and they found that "it is difficult to interpret the morphology observed in I22023 in the framework of the standard interacting stellar wind (ISW) model (e.g., Kwok et al. 1978), even invoking a strong density gradient in the nebula. For this object, a jet would be more likely the source of the observed morphology".

5 DISCUSSION AND CONCLUSIONS

Our analysis of the high-resolution (R \sim 50,000) optical spectrum of I22023 together with our detailed line identifications confirm that I22023 is a hot (B-type) O-rich post-AGB star (see below). That I22023 is not a normal population I B star is also suggested by the large heliocentric radial velocity of the star (-148.31 ± 0.60 km s $^{-1}$)¹, as measured from the absorption lines present in its high-resolution optical spectrum. Thus, it is more likely that I22023 is a post-AGB star belonging to the old disk population. The presence of absorption lines of He I, C III, Si III together with [N II], [O I], and [S II] emission lines indicate a low-excitation nebula surrounding the early B-type central star. The observed P-Cygni profiles in the lines of hydrogen, He I, C II, and Fe III clearly indicate the presence of a stellar wind with a significant post-AGB mass-loss rate, providing strong evidence for on-going post-AGB mass loss.

As a first approximation, using LTE analysis, we estimated $T_{\text{eff}} = 24,000 \text{ K} \pm 1000 \text{ K}$, $\log g = 3.0 \pm 0.5$ and $\xi_t = 7 \pm 1$ km s $^{-1}$. The derived CNO abundances are compared with the average CNO abundances for main-sequence B-stars from the Ori OB1 association (Kilian 1992) in Table 6. The CNO abundances indicate that I22023 is an evolved star. We estimated C/O \sim 0.48, implying that the central star is O-rich and that the C/O ratio was not altered during the previous AGB phase. Our Si abundance estimate also suggests that I22023 is only slightly metal-deficient with [Si/H] $=-0.12\pm0.10$. Our derived abundances can be easily

explained if I22023 is the descendant of a low-mass (e.g., below $\sim 1.5 M_{\odot}$) AGB star of roughly solar metallicity. Low-mass stars evolve very slowly and are expected to remain O-rich all the way along the AGB because they experience too few thermal pulses and the third dredge-up is too inefficient² to modify the original C/O < 1 ratio (see e.g., Herwig 2005 for a review). However, intermediate-mass ($1.5 < M < 3-4 M_{\odot}$) AGB stars are converted to carbon and s-process enriched stars (see below) while massive ($M > 3-4 M_{\odot}$) AGB stars remain also O-rich as a consequence of the Hot Bottom Burning (HBB) activation and experience a completely different s-process nucleosynthesis (see e.g., García-Hernández et al. 2006a, 2007a, and references therein). Note that the low-mass interpretation for I22023 would be consistent with the fact that I22023 is an optically bright O-rich post-AGB star while more massive O-rich post-AGB stars (which experienced HBB in the AGB) usually are completely obscured in the optical range by their thick circumstellar envelopes (e.g., García-Hernández et al. 2007b). In short, attending to the high-resolution spectrum of I22023 only, we may conclude that I22023 is a low-mass O-rich post-AGB star.

Even though the IRAS cool (e.g., F, G) and hot (O, B) post-AGB stars show supergiant like spectra, indicating an evolutionary sequence in the transition region from the AGB to the PN stage, they seem to show fundamental differences in their chemical compositions. In the high Galactic latitude hot (O-, B-type) post-AGB stars, a severe carbon deficiency (i.e., C/O<1) is detected indicating that they left the AGB before the third dredge-up (e.g., Conlon et al. 1991; McCausland et al. 1992; Moehler & Heber 1998) has enriched the stellar surface with the products of the complex nucleosynthesis (e.g., carbon and heavy s-process elements such as Rb, Zr, Y, Sr, etc.) experienced during the AGB phase (see e.g., García-Hernández et al. 2007a and references therein). A similar carbon deficiency is also detected in the hot post-AGB stars in globular clusters (Moehler et al. 1998; Mooney et al. 2004; Jasniewicz et al. 2004; Thompson et al. 2006). The only exception to this observational evidence is the field hot post-AGB star, IRAS 01005+7910, which shows an overabundance of carbon (Klochova et al. 2002). In contrast, among the IRAS selected cool (F-, G-type) post-AGB stars there is a majority of post-AGB stars in which a severe carbon deficiency is not detected. The F-, G-type post-AGB stars with the still unidentified 21 micron emission feature show an overabundance of carbon and heavy s-process elements (e.g., Van Winckel & Reyniers 2000), confirming that they have experienced s-process nucleosynthesis and the third dredge-up in the previous AGB phase and that they evolved from intermediate-mass carbon stars.

Interestingly, Cerrigone et al. (2009) found that I22023 is a double-dust chemistry - i.e., it displays the simultaneous presence of both C-rich and O-rich dust features - post-AGB star from their analysis of the recent Spitzer mid-infrared ($\sim 5-40 \mu\text{m}$) spectrum of I22023. The mixed-chemistry is deduced from the detection of amorphous silicates emission at ~ 10 microns together with the classical aromatic infrared

¹ Note that the high radial velocity suggests that I22023 is an old disk low core mass post-AGB star and that there are old disk stars whose chemical composition is close to the solar composition (Furhmann 1998, 2004).

² Note also that theoretical models predict a higher efficiency of the dredge-up in low metallicity atmospheres with respect to those with solar metallicity (e.g. Lugaro et al. 2003).

Table 8. Expansion velocities

Ident.	λ_{lab} Å	FWHM Å	V_{exp} km s ⁻¹
6300.23	[OI](1F)	1.334	31.76
6363.88	[OI](1F)	1.470	34.65
6548.1	[NII](1F)	0.844	19.34
6717.0	[SII](2F)	0.747	16.68
6731.3	[SII](2F)	0.739	16.47

bands (AIBs; e.g., at ~ 6.2 , 7.7 , 8.6 , and $11.3 \mu\text{m}$) usually attributed to carbonaceous compounds. The origin of the double-dust chemistry is still not very well understood and several scenarios, including the presence of a binary central system, a late thermal pulse on the AGB or post-AGB phases, HBB cessation by extreme mass loss, etc., have been proposed to explain the mixed-chemistry phenomenon observed in AGB stars (e.g., García-Hernández et al. 2006b), post-AGB stars (e.g., Waters et al. 1998; Gielen et al. 2011), and PNe (e.g., Perea-Calderón et al. 2009).

The presence of carbonaceous molecules in an O-rich environment such as that in I22023 (the central star is also O-rich!) is surprising and puzzling. Cerrigone et al. (2009) propose that the mixed-chemistry in I22023 (and other hot post-AGB stars) is due to the presence of a circumbinary disk/torus where O-bearing molecules would be preserved from the 3rd dredge-up, while the C-bearing molecules would be formed elsewhere in the outflow. The presence of a binary companion in I22023 and other hot post-AGB stars cannot be ruled out. Indeed, the presence of a close companion (at a distance of $\sim 0.4''$) in the proto-type hot post-AGB object Hen 3-1357 (the “Stingray Nebula”) is well known (Bobrowsky et al. 1998). In addition, an spectacular incipient bipolar morphology is clearly seen in the HST images of Hen 3-1357. The Spitzer spectrum of Hen 3-1357 (see Perea-Calderón et al. 2009) resembles that of I22023, showing amorphous silicates emission at $10 \mu\text{m}$ together with a strong IR continuum but only a weak carbonaceous emission at $11.3 \mu\text{m}$ is seen; there is a complete lack of the other AIBs at ~ 6.2 , 7.7 , and $8.6 \mu\text{m}$. In this context, the likely incipient bipolar morphology observed in I22023 (Volk et al. 2004) would support the presence of a binary companion.

On the other hand, the most recent idea to explain the mixed-chemistry phenomenon is from Guzmán-Ramírez et al. (2011). These authors propose a chemical model able to form hydrocarbon chains in an UV-irradiated dense torus in order to explain the high detection rate of mixed-chemistry in PNe of the Galactic Bulge. However, the UV radiation field in I22023 ($T_{\text{eff}}=24,000 \text{ K}$) is lower than that in double-dust chemistry PNe (with $T_{\text{eff}}>34,000 \text{ K}$) and may be not intense enough to efficiently break the CO molecules. In addition, the Spitzer infrared spectrum of I22023 is very peculiar because the O-rich silicate dust is mostly amorphous and there is no clear evidence for the presence of crystalline silicate features at wavelengths longer than $20 \mu\text{m}$. This is in strong contrast with the Spitzer spectra of double-dust chemistry PNe (e.g., Perea-Calderón et al. 2009; Guzmán-Ramírez et al. 2011) where only crystalline silicates are detected.

An alternative explanation to explain the presence of

carbonaceous molecules in I22023 may be non-equilibrium chemistry induced by shocks (Cherchneff 2011). Cherchneff (2011) demonstrates that water can form in C-rich evolved stars, showing that, independently of the stellar C/O ratio, thermal fragmentation of CO occurs in the hot post-shock gas. Our optical spectrum of I22023 shows clear evidences of on-going mass loss - i.e., the presence of a strong and variable stellar wind and shocks - which would support this carbonaceous molecules formation scenario. Indeed, other hot (B-type) post-AGB stars such as IRAS 20462+3416 and IRAS 19336-0400 are infrared spectroscopic twins of I22023, showing both an identical (mixed-chemistry) Spitzer spectrum (see Cerrigone et al. 2009) together with clear indications (e.g., P-cygni profiles) of on-going (and variable) mass loss (see Sanchez-Contreras et al. 2008; Arkhipova et al. 2011). In this scenario, the lack of strong infrared features from carbonaceous molecules in other hot and O-rich post-AGB stars such as IRAS 18062+2410 (or even the very young PN Hen 3-1357)³ would be related with the inactivity of strong stellar winds with significant mass loss rates; i.e., the absence of strong shocks activating non-equilibrium chemistry.

In summary, we speculate that the simultaneous presence of carbonaceous molecules and amorphous silicates in I22023 and other hot (B-type) post-AGB stars may point to a binary central system with a dusty disk/torus as the stellar origin common to the hot post-AGB stars hosting O-rich central stars. The episodic character of the stellar wind (shocks) and mass loss in these hot O-rich post-AGB stars would favor shock-induced non-equilibrium chemistry as the carbonaceous molecules formation scenario in these O-rich environments. Further monitoring studies (e.g., monitoring of radial velocity, light variations, strengths and profiles of emission and absorption lines) of this star and other hot post-AGB stars are encouraged in order to understand the circumstellar mixed-chemistry, mass loss rate (and evolution) with the ultimate goal of unveiling the stellar origin of this intriguing class of O-rich post-AGB objects.

ACKNOWLEDGMENTS

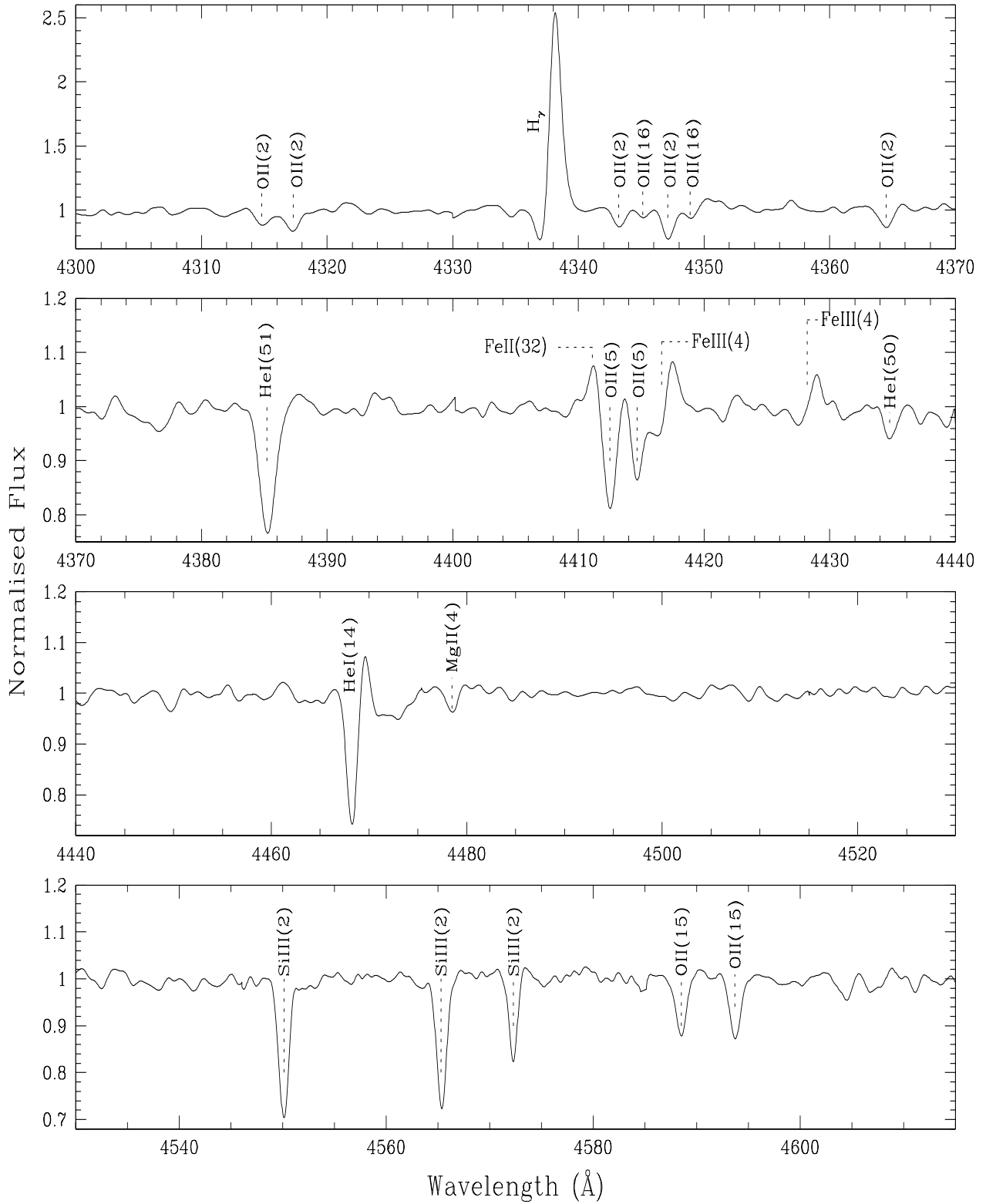
GS would like to acknowledge financial support from the Department of Science and Technology (DST), Govt. of India through a grant numbered SR/FTP/PS-67/2005 . D.A.G.H and A.M. also acknowledge support for this work

³ No P-cygni profiles (i.e., strong stellar winds) are present in IRAS 18062+2410 (Arkhipova et al. 2007) and based on the C IV 1550 Å line in the IUE UV spectrum, the fast wind in Hen 3-1357 was stopped in 1995 (Parthasarathy et al. 1995).

provided by the Spanish Ministry of Science and Innovation (MICINN) under a JdC grant and under grant AYA-2007-64748. MP is very thankful to Prof. Shoken Miyama for his kind support, encouragement and hospitality.

REFERENCES

- Arhipova, V. P., Klochkova, V. G., Sokol, G. V., 2001, *AstL*, 27, 99
- Arhipova, V. P., Ikonnikova, N. P., Komissarova, G. V., Noskova, R. I. 2006, in *Planetary Nebulae in our Galaxy and Beyond*, IAU Symp.#234, Eds. Michael J. Barlow and Roberto H. Méndez, pp. 357
- Arhipova, V. P., Esipov, V. F., Ikonnikova, N. P. et al. 2007, *AstL*, 33, 604
- Arhipova, V. P., Burlak, M. A., Esipov, V. F. et al. 2011, *AstL* (in press; arXiv: 1111.2408)
- Bakker, E. J., Waters, L. B. F. M., Lamers, H. J. G. L. M. et al. 1996, *A&A*, 310, 893
- Blöcker, T., Herwig, F., Driebe, T., 2000, *MmSAI*, 71, 711
- Bobrowsky, M., Sahu, K. C., Parthasarathy, M., García-Lario, P., 1998, *Nature*, 392, 469
- Cerrigone, L., Hora, J. L., Umana, G., & Trigilio, C., 2009, *ApJ*, 703, 585
- Cerrigone, L., Umana, G., Trigilio, C., Leto, P., Buemi, C. S., & Hora, L., 2008, *MNRAS*, 390, 363
- Cherchneff, I. 2011, *A&A*, 526, L11
- Conlon, E. S., Dufton, P. L., Keenan, F. P., & McCausland, R. J. H., 1991 *MNRAS*, 248, 82
- Friedman, S. D. et al. 2011, *ApJ*, 727, 33
- Furhmann, K., 1998, *A&A*, 338, 161
- Furhmann, K., 2004, *AN*, 325, 3
- García-Hernández, D. A., García-Lario, P., Plez, B. et al. 2006a, *Science*, 314, 1751
- García-Hernández, D. A., Abia, C., Manchado, A., García-Lario, P. 2006b, *A&A*, 452, 1049
- García-Hernández, D. A., García-Lario, P., Plez, B. et al. 2007a, *A&A*, 462, 711
- García-Hernández, D. A., Perea-Calderón, J. V., Bobrowsky, M., García-Lario, P. 2007b, *ApJ*, 666, L33
- García-Lario, P., Manchado, A., Pych, W., Pottasch, S. R. 1997a, *A&AS*, 126, 479
- García-Lario, P., Parthasarathy, M., de Martino, D. et al. 1997b, *A&A*, 326, 1103
- Gauba, G. & Parthasarathy, M. 2003, *A&A*, 407, 1007
- Gauba, G. & Parthasarathy, M. 2004, *A&A*, 417, 201
- Gielen, C., Cami, J., Bouwman, J. et al. 2011, *A&A* (in press; arXiv:1110.5996)
- Guzmán-Ramírez, L., Zijlstra, A. A., Níchuimín, R. et al. 2011, *MNRAS*, 414, 1667
- Herwig, F. 2005, *ARA&A*, 43, 435
- Hobbs, L. M. et al. 2008, *ApJ*, 680, 1256
- Hog, E. Fabricius, C., Makarov, V. V. et al. 2000, *A&A*, 355, L27
- Hubeny, I., Stefl, S., & Harmanec, P. 1985, *Bull. Astron. Inst. Czechosl.*, 36, 214
- Jasniewicz, G., de Laverny, P., Parthasarathy, M. et al. 2004, *A&A*, 423, 353
- Kilian, J. 1992, *A&A*, 262, 171
- Kelly, D. M. & Hrivnak, B. J. 2005, *ApJ*, 629, 1040
- Klochkova, V. G., Yushkin, M. V., Miroshnichenko, A. S. et al. 2002, *A&A*, 392, 143
- Kwok, S., Purton, C. R. & Fitzgerald, P. M. 1978, *ApJ*, 219, L125
- Leitherer, C. 1988, *ApJ*, 326, 356
- Lugaro, M., Herwig, F., Lattanzio, J. C. et al. 2003, *ApJ*, 586, 1305
- Luna, R., Cox, N. L. J., Satorre, M. A. et al. 2008, *A&A*, 480, 133
- McCausland, R. J. H., Conlon, E. S., Dufton, P. L., Keenan, F. P. 1992, *ApJ*, 394, 298
- Moehler, S. & Heber, U. 1998, *A&A*, 335, 985
- Moehler, S., Heber, U., Lemke, M., Napiwotzki, R. 1998, *A&A*, 339, 537
- Mooney, C. J., Rolleston, W. R. J., Keenan, F. P. et al. 2004, *A&A*, 419, 1123
- Moore, C. E. 1945, *A multiplet table of astrophysical interest* part - I, Table of Multiplets revised ed. (Princeton, Princeton Univ. Obs.)
- Omont, A., Loup, C., Forveille, T. et al. 1993, *A&A*, 267, 515
- Osterbrock, D. E., Fulbright, J. P., Martel, A. R. et al. 1996, *PASP*, 108, 277
- Parthasarathy, M., Pottasch, S. R. 1986, *A&A*, 154, L16
- Parthasarathy, M., Pottasch, S. R. 1989, *A&A*, 225, 521
- Parthasarathy, M., 1993, *ApJ*, 414, L109
- Parthasarathy, M., García-Lario, P., Pottasch, S. R. et al. 1993 *A&A*, 267, L19
- Parthasarathy, M., García-Lario, P., de Martino, D. et al. 1995, *A&A*, 300, L25
- Parthasarathy, M., Vijapurkar, J., Drilling, J. S. 2000a, *A&AS*, 145, 269
- Parthasarathy, M., García-Lario, P., Sivarani, T. et al. 2000b, *A&A*, 357, 241
- Perea-Calderón, J. V., García-Hernández, D. A., Bobrowsky, M. et al. 2009, *A&A*, 495, L1
- Pottasch, S. R., Parthasarathy, M. 1988, *A&A*, 192, 182
- Ryans, R.S.I., Dufton, P.L., Mooney, C.J., et al. 2003, *A&A*, 401, 1119
- Sánchez Contreras, C., Sahai, R., Gil de Paz, A., Goodrich, R. 2008, *ApJS*, 179, 166
- Sarkar, G., Parthasarathy, M., Reddy, B. E. 2005, *A&A*, 431, 1007
- Sahai, R., Sánchez Contreras, C., Morris, M. 2005, *ApJ*, 620, 948
- Schlegel, D. J., Finkbeiner, D. P., & Davis, M. 1998, *ApJ*, 500, 525
- Thompson, H. M. A., Keenan, F. P., Dufton, P. L. et al. 2006, *MNRAS*, 368, 1749
- Van Winckel, H., & Reyniers, M. 2000, *A&A*, 354, 135
- Volk, K., Hrivnak, B. J., Kwok, S. 2004, *ApJ*, 616, 1181
- Wackerling, L. R. 1970, *Mem. Roy. Astron. Soc.*, 73, 153
- Waters, L. B. F. M., Molster, F. J., de Jong, T. et al. 1996, *A&A*, 315, L361
- Welch, C. A., Frank, A., Pipher, J. L., Forrest, W. J., 1999, *ApJ*, 522, L69

HIGH RESOLUTION OPTICAL SPECTRUM OF IRAS 22023+5249**Figure 4.** Optical spectrum of IRAS22023+5249 (LS III +52°24)

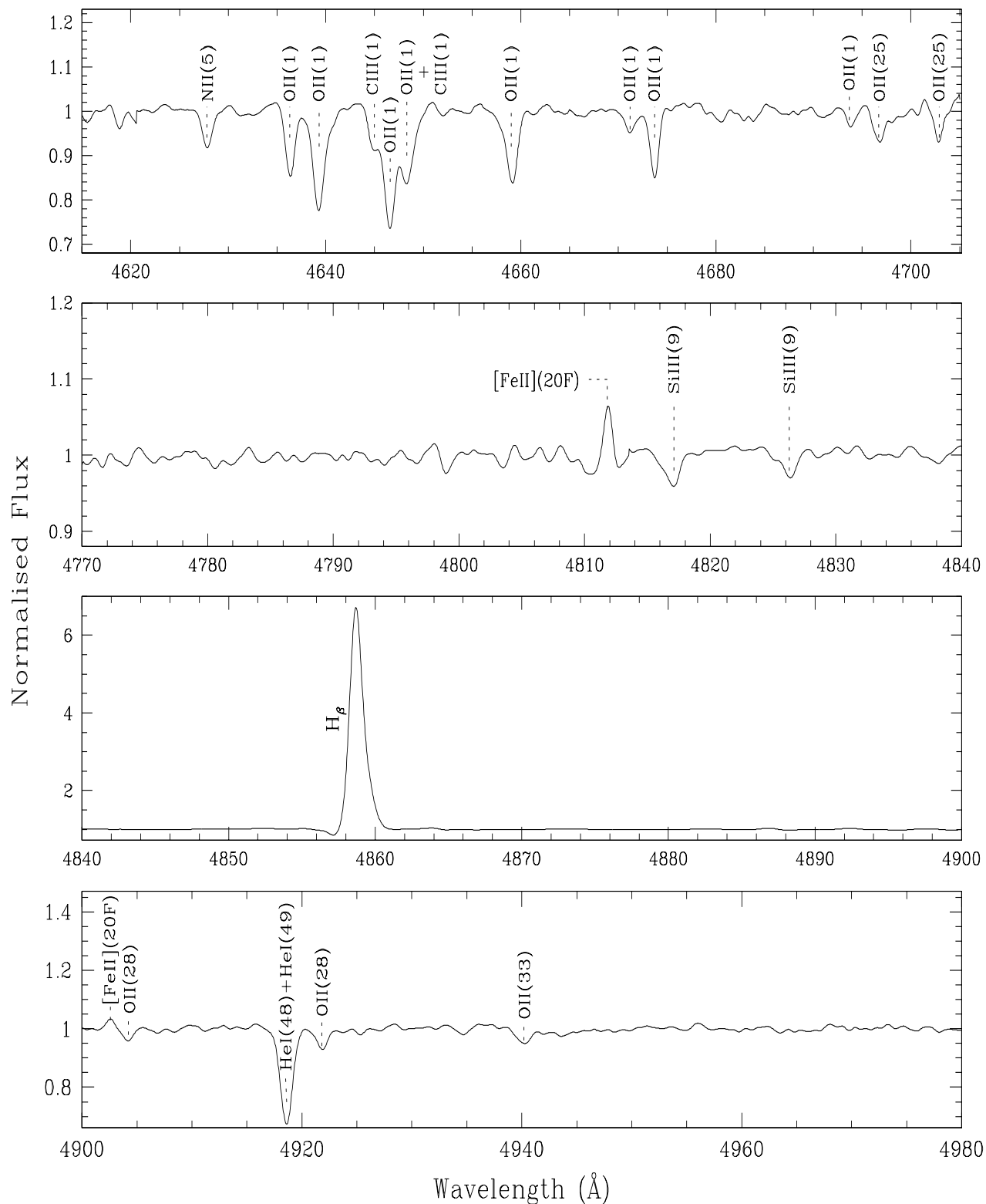
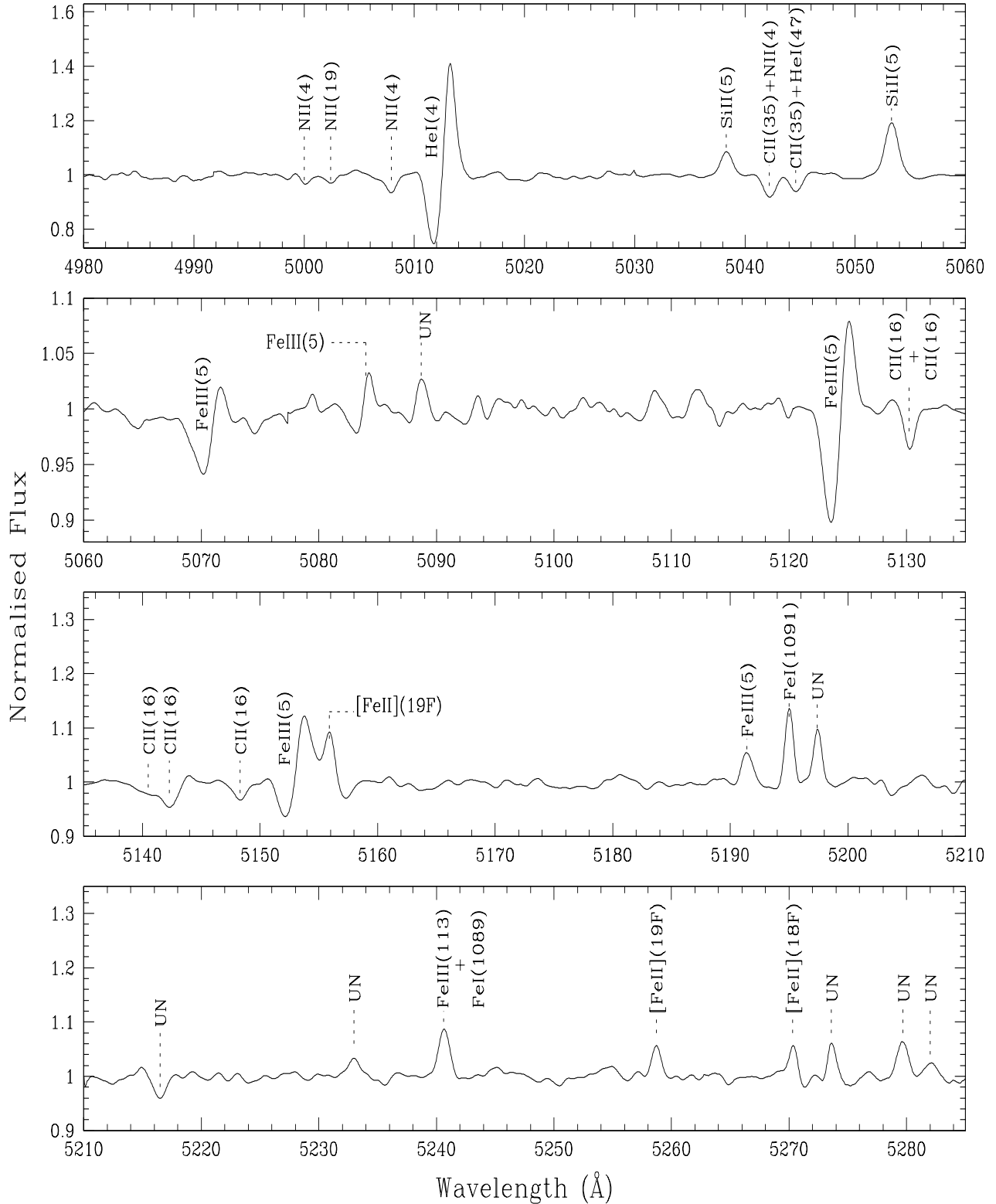


Figure 4. Optical spectrum of IRAS22023+5249 (LS III +52°24) contd...

**Figure 4.** Optical spectrum of IRAS22023+5249 (LS III +52°24) contd...

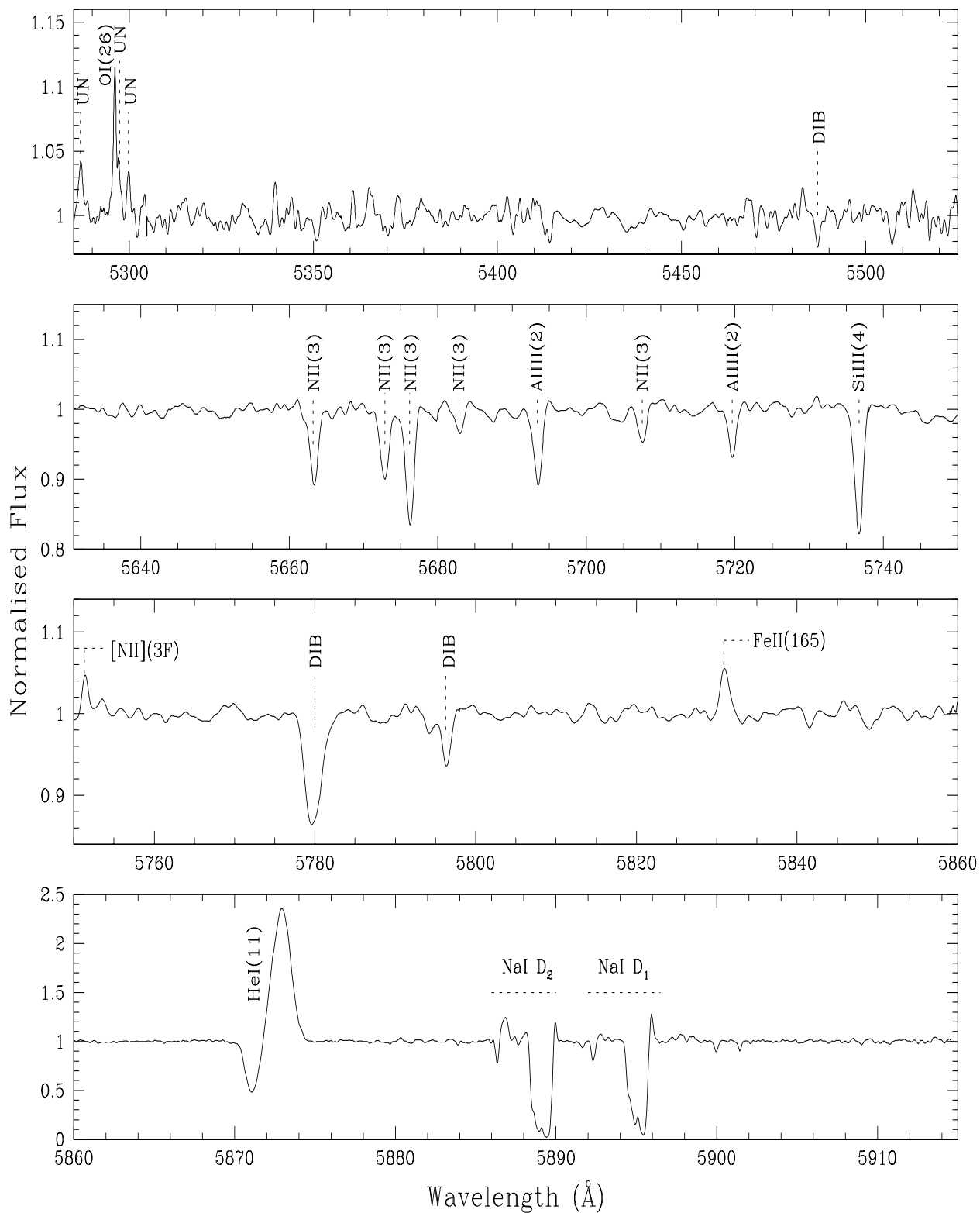


Figure 4. Optical spectrum of IRAS22023+5249 (LS III +52°24) contd...

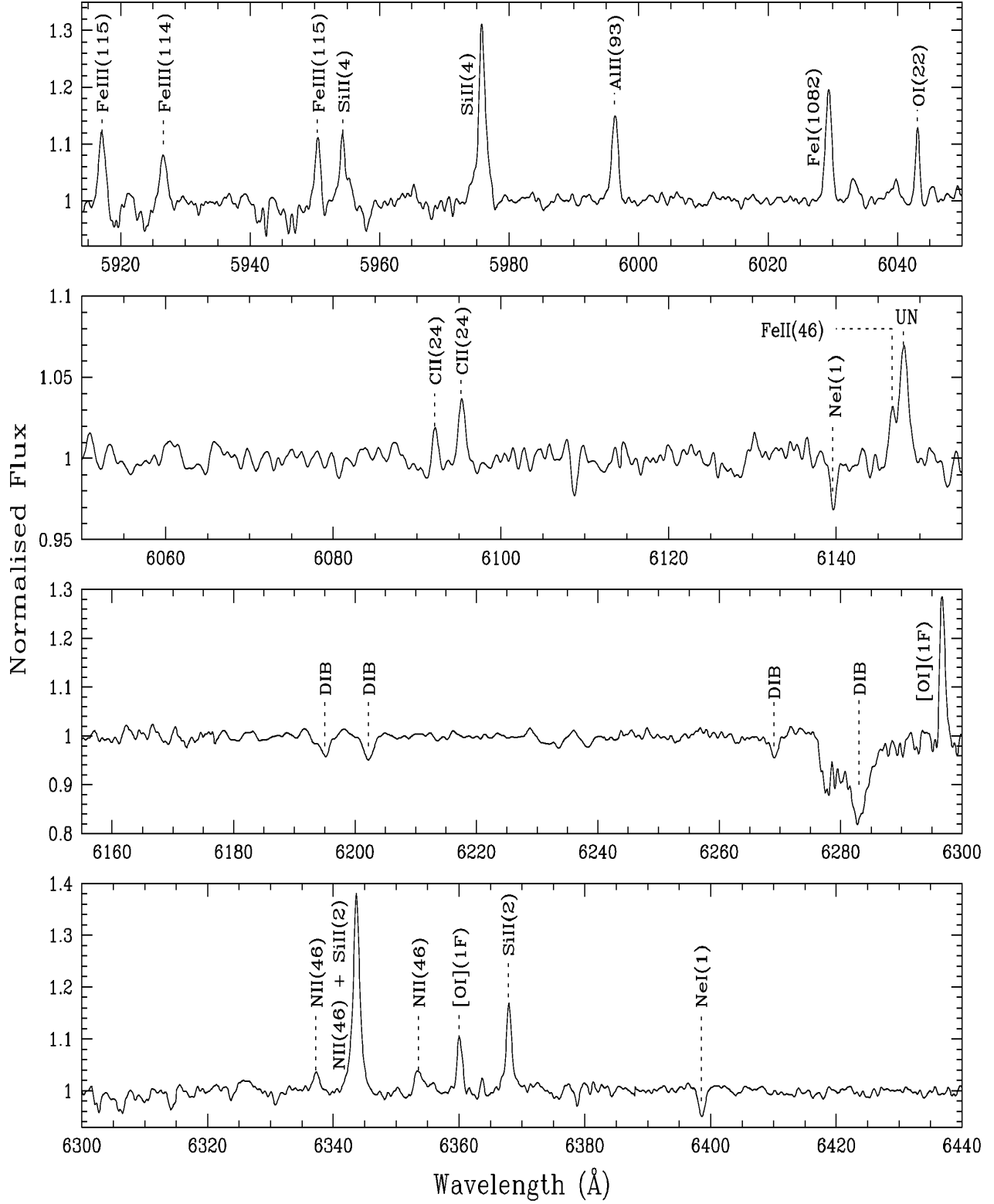


Figure 4. Optical spectrum of IRAS22023+5249 (LS III +52°24) contd...

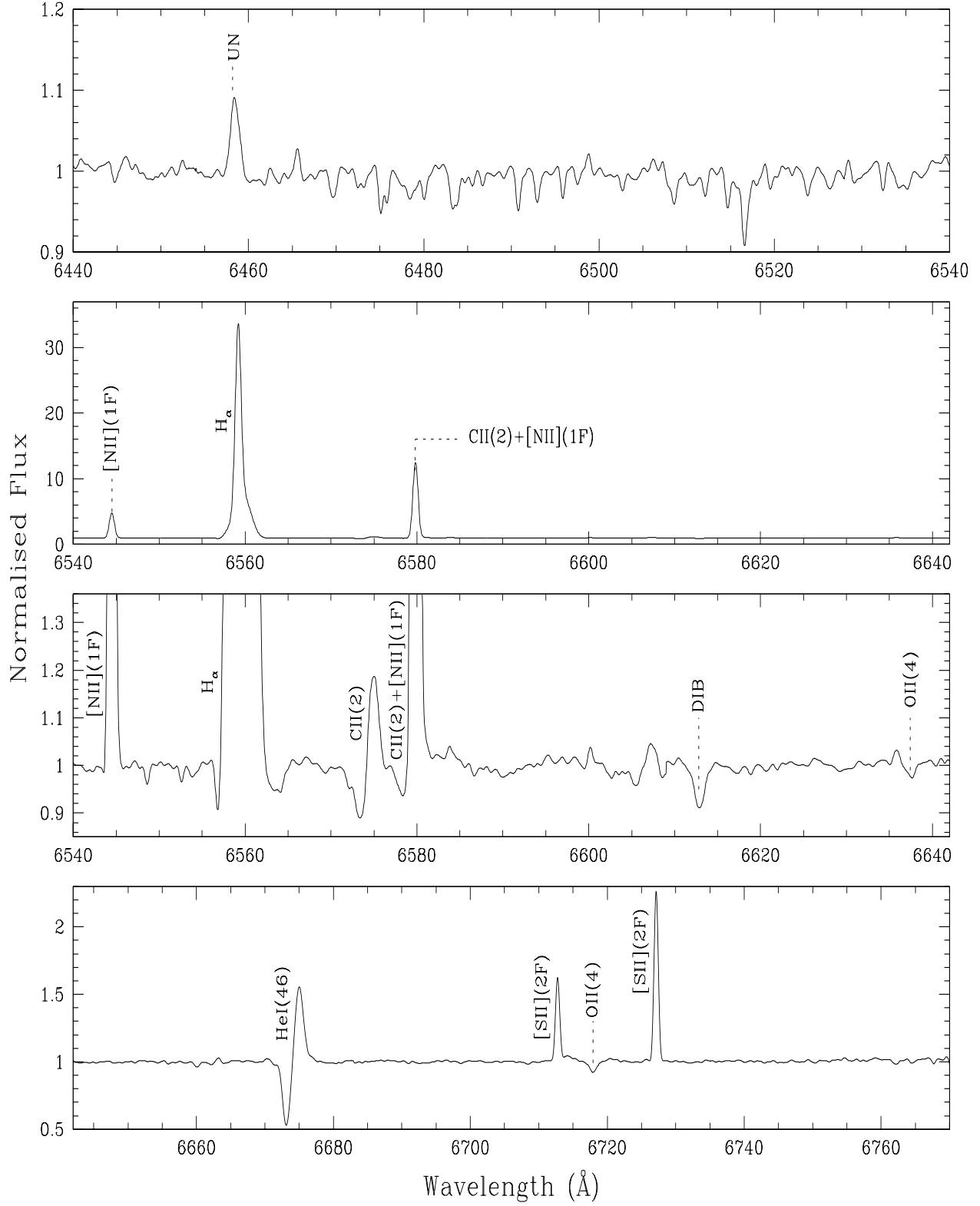


Figure 4. Optical spectrum of IRAS22023+5249 (LS III +52°24) contd...

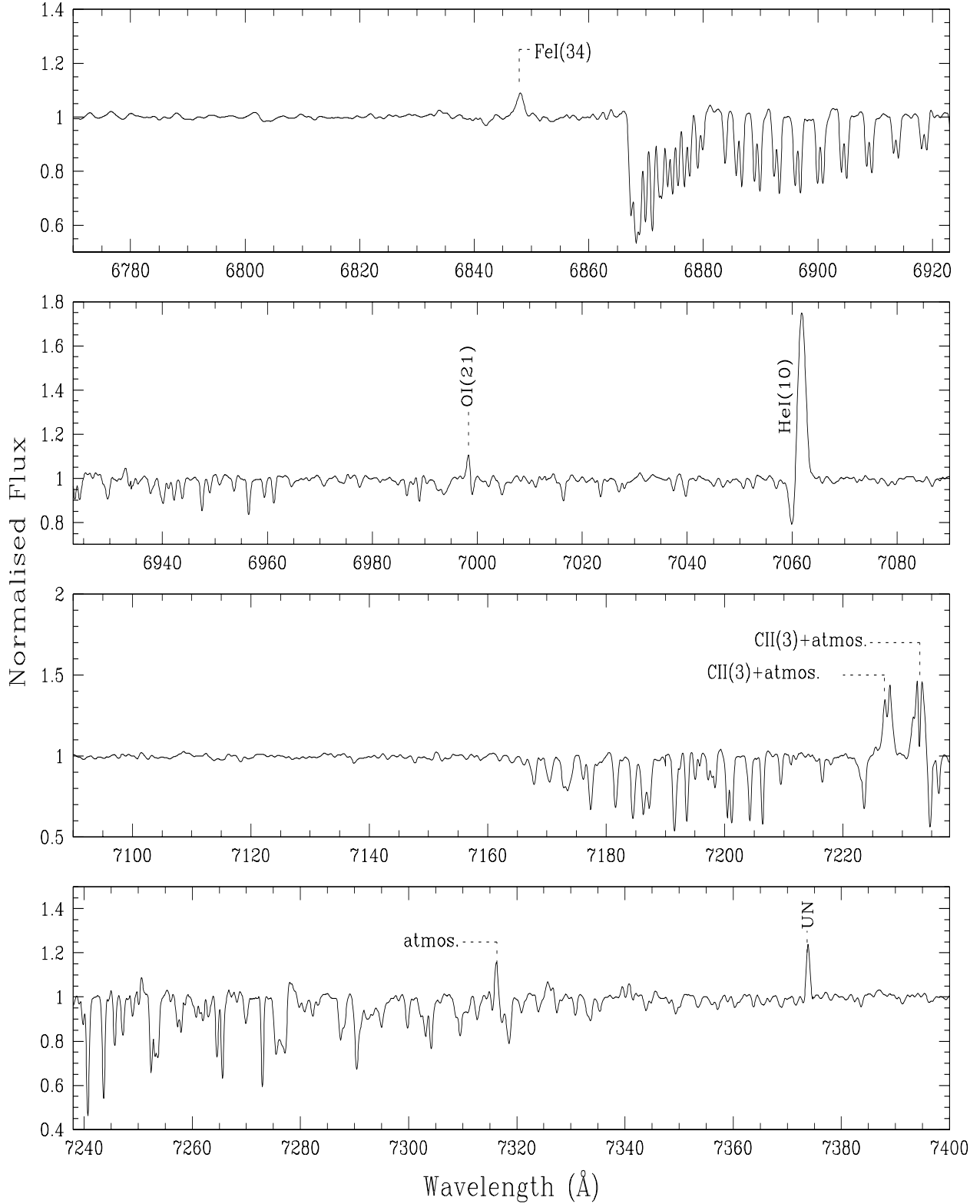


Figure 4. Optical spectrum of IRAS22023+5249 (LS III +52°24) contd...

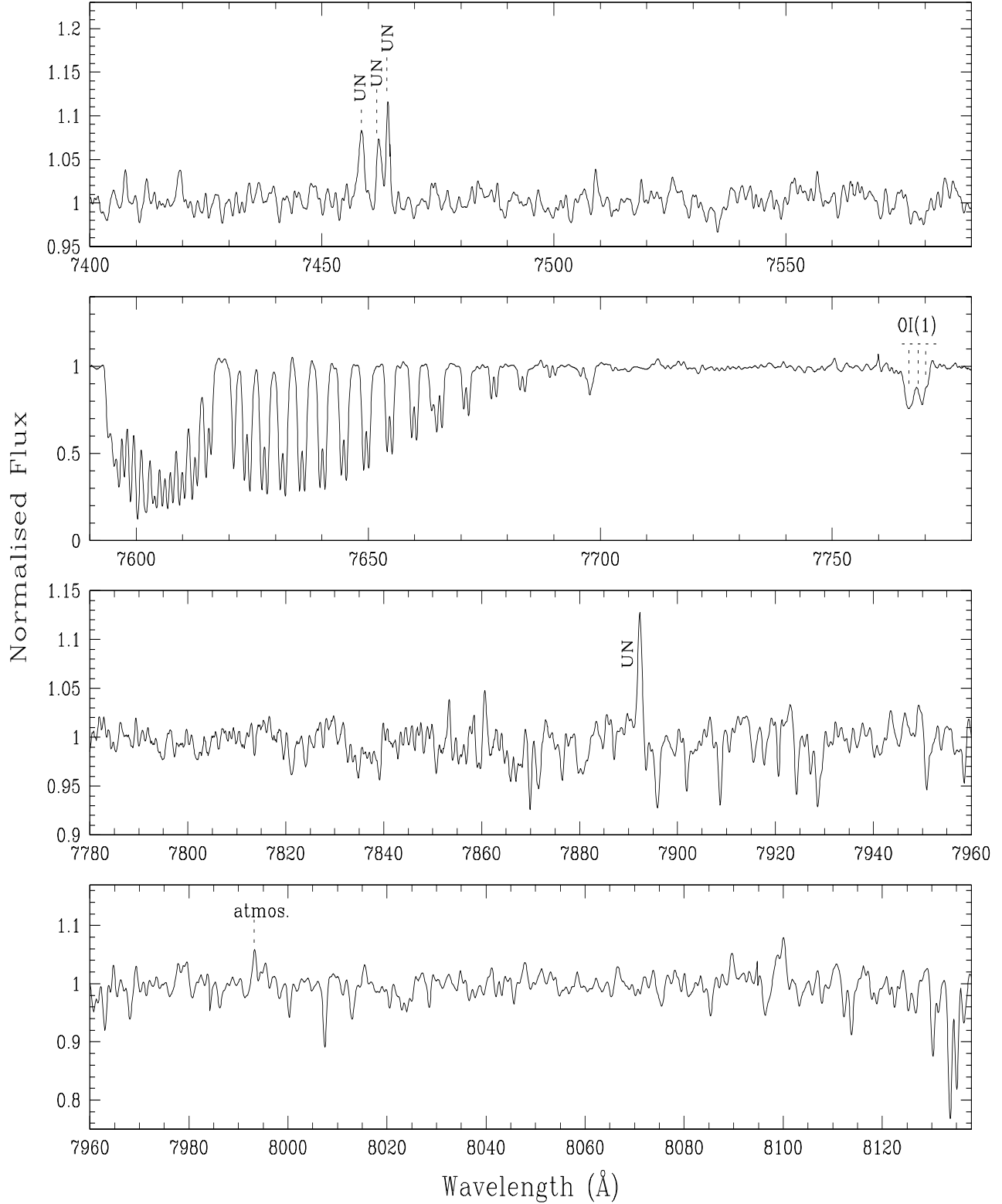


Figure 4. Optical spectrum of IRAS22023+5249 (LS III +52°24) contd. Note that the unmarked absorption line around 7698 Å is interstellar K I.

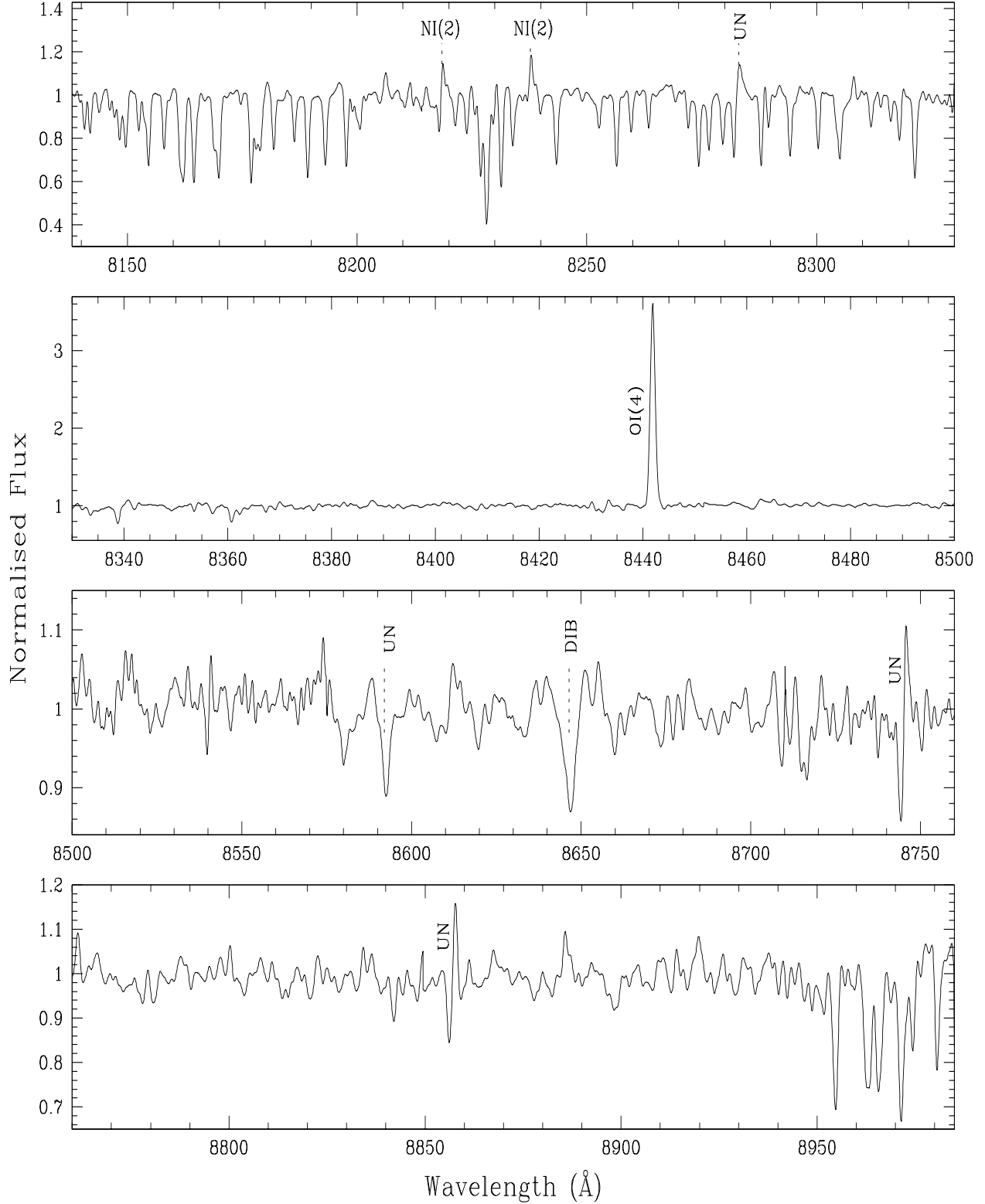


Figure 4. Optical spectrum of IRAS22023+5249 (LS III +52°24) contd...

